International Conference on Space Optics—ICSO 2014

La Caleta, Tenerife, Canary Islands

7–10 October 2014

Edited by Zoran Sodnik, Bruno Cugny, and Nikos Karafolas

Evaluation of the refocusing system of the polarimetric helioseismic imager/full disk telescope of the solar orbiter mission

M. Silva-Lopez

J. A. Bonet-Navarro

A. Núñez

A. Álvarez-Herrero

esa icso proceedings cnes

International Conference on Space Optics — ICSO 2014, edited by Zoran Sodnik, Nikos Karafolas, Bruno Cugny, Proc. of SPIE Vol. 10563, 1056360 · © 2014 ESA and CNES
CCC code: 0277-786X/17/$18 · doi: 10.1117/12.2304142

EVALUATION OF THE REFOCUSING SYSTEM OF THE POLARIMETRIC HELIOSEISMIC IMAGER/FULL DISK TELESCOPE OF THE SOLAR ORBITER MISSION

M. Silva-López[1], J. A. Bonet-Navarro[2], A. Nuñez[1], A. Álvarez-Herrero[1]
[1]*Instituto Nacional de Técnica Aeroespacial, Área de Instrumentación Óptica Espacial, Madrid, Spain.*
[2]*Instituto Astrofísico de Canarias, San Cristóbal de La Laguna, Spain*

ABSTRACT

The Full Disk Telescope is part of the Polarimetric Helioseismic Instrument on board the future Solar Orbiter ESA/NASA mission. The Full Disk Telescope will provide for full-disk measurements of the photospheric vector magnetic field and line-of-sight velocity, as well as the continuum intensity in the visible wavelength range. Along this mission, it is expected that thermal drifts will induce image focus displacements. Consequently, providing an autofocus system is mandatory to prevent image degradation. The refocusing system is based on an autonomous image quality analysis and it allows for a lens displacement in order to locate the best focus position. In this document the system and the figure of merit chosen for the image quality evaluation is presented. The algorithm is a gradient based contrast and it is adapted to the object features. Moreover, the telescope is not equipped with image stabilization system and therefore attitude stability must be assessed. Jitter is modelled as a circular normal distribution of the pointing direction. A stability of 0.5 arcsec (σ_ρ) during frame accumulation is simulated and its impact on image contrast evaluated. Considering this jitter, image contrast is only reduced to 99.8% the contrast of an unaffected image. Finally, to estimate the effect in the process performance, the mechanical uncertainties expected for the linear actuator were added to the defocus due to the lens excursion. The results show that the proposed refocusing system is sufficiently robust against the expected image shifts and mechanical instabilities.

I. INTRODUCTION

The future Solar Orbiter (SolO) ESA/NASA mission is intended to perform measurements of the inner heliosphere, nascent solar wind, and close observations of the polar regions of the Sun [1]. It will reach a perihelion of 0.28 astronomical units (AU) and orbit up to 34º out of the ecliptic. The spacecraft is a Sun-pointed, 3-axis stabilized platform, with a dedicated heat shield to provide protection from the high levels of solar flux near perihelion. Its payload suit combines remote sensing with in-situ analysis instrumentation. Suitable fields-of-view to the Sun are provided for the remote-sensing instruments by means of feedthroughs in the heat shield.

The Polarimetric and Helioseismic Imager (PHI) is one of the remote sensing instruments on board the SolO. PHI is a high resolution spectrometer, a high sensitive polarimeter and a diffracion-limitted imager that will perform polarimetric measurements of the solar surface. It is an instrument with complex subsystems. Within PHI, two telescopes work sequentially: The Full Disk Telescope (FDT) and the High Resolution Telescope (HRT). Both telescopes rely on an autofocus capability to precisely focus on the Sun, and compensate for thermal/vacuum environment defocusing effects that could be encountered during the mission.

In particular, the FDT Re-focussing Mechanism (FRM), is designed to adjust the optics of the FDT to obtain focused images at the scientific focal plane. This, as any mechanism, will suffer from position uncertainties due to wearing and backlash, and its precision will affect the performance of the refocusing process. A similar arrangement has been successfully employed in Martian environment conditions [2]. These conditions are very different from interplanetary vacuum conditions, however some requirements are typical, such as strong restrictions on mass and power consumption, robustness, etc... Moreover, PHI is expected to suffer from jitter in the spacecraft. Images from HRT are compensated by a correlation tracker mechanism and a closed loop real-time image motion compensation by a tip/tilt mirror. That provides for an image stabilization system. However, the FDT, with comparatively relaxed requirements, lacks this system and the jitter influence must be evaluated.

In this paper the FRM is presented. This is an optomechanical assembly designed to hold two lenses, plus the entrance diaphragm of the FDT system. One of these lenses, mounts on a motorized platform, which locates it at the exact point to perform the correct focusing of the system at any situation. Image quality degradation is simulated and the influence of mechanical effects, such as the jitter and the mechanical uncertainties, are modelled and evaluated. Then, a number of images, related to the lens position are generated. The refocussing process is finally simulated, applying a figure of merit to estimate the contrast of these images, and find the best focus position.

II. THE POLARIMETRIC AND HELIOSEISMIC IMAGER

Fig. 1 shows a CAD model of PHI. Some parts of the HRT are not shown so that the FDT path can be seen clearly. The location of the FRM is also indicated. The FDT optical subsystem between the FRM and M5 is mounted in a rigid tube, with M5 as an alignment mirror. The FDT tube is mounted fixed in position into the back structural element of the PHI optical unit (OU) structure, while the front end of the tube is allowed to expand in axial direction (to allow for differential thermal expansion of the aluminium tube and the carbon fiber struts of the structure). This is achieved via radially mounted flex blades between the front end of the FDT tube and the front structural block. The instrument feet are connected to the blocks.

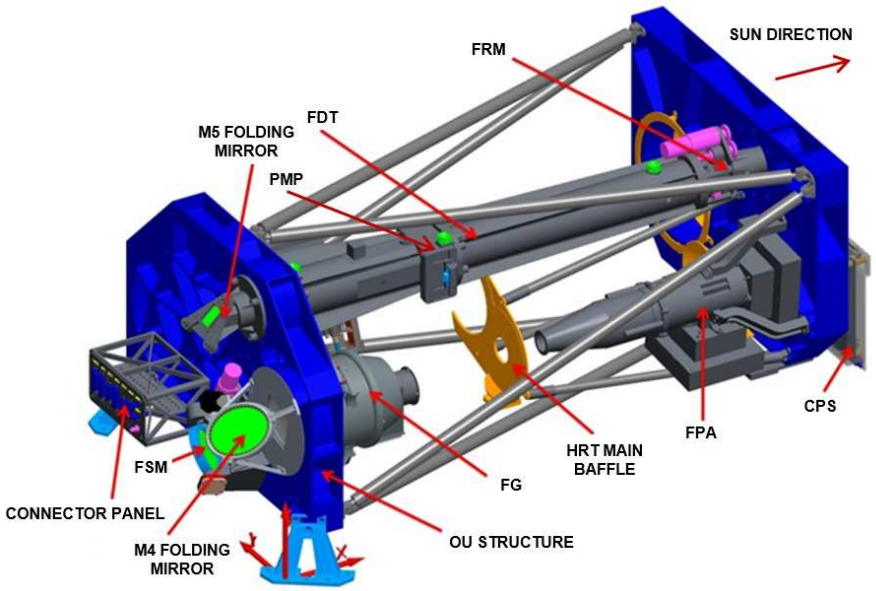

Fig. 1. CAD model of the PHI optical unit. Some sections of the HRT are not shown so that the FDT can be seen clearly. The FRM is one section of the FDT assembly.

The FDT is connected to the common branch of PHI via the folding mirror M5 and by action of the feed selection mechanism (FSM). Thus, the two telescopes can work sequentially and their selection is made by the FSM, which feeds one filtergraph (FG), the camera optics and one focal plane array (FPA). The FG provides for a very narrow passband filter centered at a wavelength of λ=617 nm. The polarimetric analysis is performed by one polarization modulation package (PMP) [3] in each of the telescopes. The modulation scheme is the same as the one used in the IMaX instrument of the Sunrise mission [4]. Both telescopes apertures are protected by intense solar flux by special heat rejecting entrance windows, which are part of the heat-shield assembly [5,6]. The FDT is designed as a refractive telescope and, as its name suggests, it will yield full disk images of the Sun with ±1° FOV of circular aperture and 17.5 mm diameter. The detector is a 2048×2048 pixel CMOS array with a 10 µm pixel size. An effective focal length of 579 mm yields to a ~3.5 arcsec per pixel of angular resolution, and a depth of focus of ±1.35 mm at the FPA.

III. FDT REFOCUS MECHANISM

The mechanical parts of the FRM are shown in Fig. 2a). Movement is originated on a two-phase stepper motor (Phytron VSS26), designed for extreme environmental applications and coupled to a 7:1 reduction gear. The output shaft is finally connected to a leading screw with a lead pitch of 1 mm clamped to the movable platform. Linear displacement is ensured by a mobile plate guided by miniature railways with 45º crossed rollers. Two end of travel limit switches are used to set the scanning range. They are also used to set the zero at the longitudinal axis, and as a reference in case step count is lost by electronics. Moreover, they prevent damage from accidental over travel.

The optical components are shown in the FRM cross section illustrated in Fig. 2b). These are the entrance pupil, and the lenses L1 and L2. The lens L1 is fixed at the structure of the mechanism; while the rail guides support L2, with its mechanical mount. As a consequence, L2 is moved along the optical axis, changing the optical path of the incoming Sun light, and compensating for defocus effects due to, e.g., manufacturing tolerances and temperature changes. Focus is then achieved by moving L2 with high accuracy and repeatability over a ~4 mm travel range, and in the applicable range of temperatures. An L2 shift of 80 µm can compensate

for 1 mm of focus displacement at the FPA. Therefore, the system is able to compensate for strong defocused situations.

An L2 displacement of ±110 µm covers the FDT depth of focus. Then, since the whole travel range of the lens is 4 mm, we have chosen to cover this range by scanning it in steps of Δz = 110 µm (hence 37 steps). The method proposed for the refocusing process is based on acquiring a sequence of images during the scan of L2 along the optical axis. Processing of the images is performed and L2 is located where image contrast was measured higher. For the mechanism, a ±10 µm uncertainty position is defined.

Along the SolO science mission orbital period phase, of 168 days, the FRM is expected to reach temperatures between -17ºC and +63ºC. From this it can be extrapolated a temperature change of ~1ºC per day. Nevertheless, once the system is focused it withstands a variation of some tens of degrees with no need to refocus, as the displacement is kept within the depth of focus. The FRM is designed to perform 1020 autofocus sequences during its lifetime.

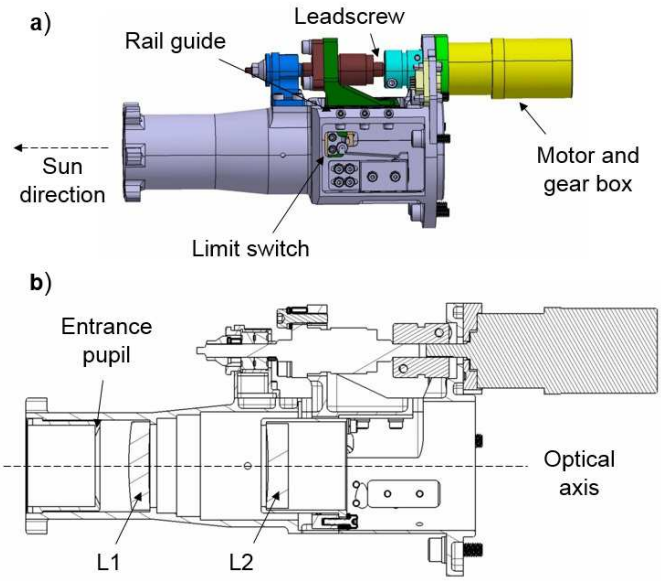

Fig. 2. FRM. a) Lateral view of the mechanism CAD model where the main parts are shown. Only one switch can be seen from the side. b) Cross section exposing the optical components.

IV. EVALUATION OF IMAGE QUALITY

To evaluate the loss of contrast in a monochrome image an algorithm based in the image gradient is used. The figure of merit employed will be the square of the gradient, which is proportional to the edge strength, i.e. the contrast [7]. Moreover, to reduce computation time and improve performance a ring-shaped mask is applied in the computation. This mask is calculated to match the image and exposes only the solar limb, as it will be explained later.

Since the algorithm is adapted to the image features, we will first describe the test image used in our numerical experiments. The image shown in Fig. 3 (left) was obtained by the Helioseismic and Magnetic Imager (HMI) on board the Solar Dynamic Observatory in Earth orbit [8]. The solar limb is clearly seen against the dark outer space and large sunspots can be seen in the solar surface. The Sun nearly fills the 4096×4096 pixel continuum intensity image. Thus, to match the PHI detector resolution and produce a reference image for our simulations, a rebinned by 2 version of this image will be used.

In our simulations, we assume a linear incoherent imaging system. Where the optical transfer function (OTF) is found by autocorrelation of the generalized pupil: $P(r)\exp(i\phi)$, with $P(r)$ the binary aperture function and ϕ the phase aberration [9, 10]. The reference image results from the multiplication of this OTF with no aberration terms, by the Fourier transform of the HMI image (i.e. only diffraction is considered). In this calculation, and in order to ensure the equivalence of the image resolution, the different orbiting distances of the HMI (1 AU) and FDT (0.28 AU) have to be taken into account. Consequently, the aperture and effective focal length of the FDT have to be scaled by a factor 0.28^{-1}. The image can be then considered to be obtained by a FDT equivalent in Earth orbit.

The algorithm employed for the contrast evaluation was the square of the gradient. This is a typical approach for edge detection, and it is based on enhancing abrupt changes of intensity [7]. Thus the figure of merit used to evaluate the contrast of a $N \times N$ pixels image I is

$$\frac{1}{\bar{I}\sum_{i,j}^{N,N} M_{i,j}} \sum_{i,j}^{N,N} \left[\left(\left(\frac{\partial I_{i,j}}{\partial x} \right)^2 + \left(\frac{\partial I_{i,j}}{\partial y} \right)^2 \right) M_{i,j} \right] \tag{1}$$

where *i* and *j*, the pixel coordinates in the image, are integers from 0 to *N*, and the derivatives are computed by finite differences. *M* is a binary mask of *N*×*N* pixels. The mask and $\bar{I}$, the mean value of the image, are dividing the masked-gradient term in order to normalise the final figure of merit.

Since the gradient is higher at the solar limb, in our study we pay special attention to this area. We thus apply the binary mask that cancels the entire image but the solar limb area. This mask is obtained by thresholding, based on *I*, and reduces the influence of changing solar prominences or sunspots on the computation. It has the shape of a ring with value 1, in the region of the limb, or where the gradient of *I* is high, and 0 elsewhere. At Fig. 3 (right), a) and b) show sections of the image, the solar limb, in focus and its corresponding mask. The width of the ring is small due to the small high contrast region. On the contrary, for a severely defocused image, like the one shown in c), a wider ring mask, illustrated in d), must be employed.

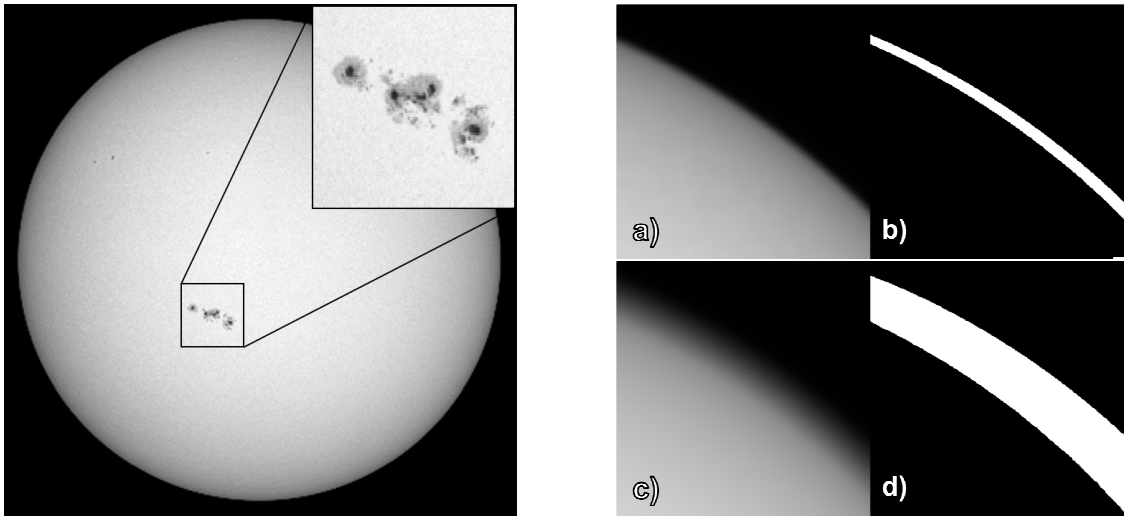

Fig. 3. Left: Sun image used as a reference for the numerical experiments. A close up of a group of sunspots are shown in the inset. Right: A section of the Sun limb in and out of focus in a) and c). Their associated masks are shown in b) and d) respectively.

Equation (1) will be the figure of merit used to evaluate contrast as a function of different image degradation factors. Its performance will be also compared to other methods in the last section.

V. JITTER SIMULATION

Random jitter in the spacecraft can lead to a loss of sharpness in the images captured, thus degrading the whole instrument performance. These random vibrations are not completely random. Their magnitude through the frequency domain is expressed in terms of power spectral density. However, expected vibrations in the platform are difficult to model or simply unknown. Sometimes, data from previous missions is employed [11], but this is not always suitable. In practice imaging stabilization systems are equipped inside telescopes when high resolution observations are required.

The FDT, on the contrary, observes the solar disk at low spatial resolution, and no ISS is included in its design. Moreover, at the spacecraft level, expected values for the jitter reported by ESA are RMS(ρ)=0.5 arcsec within 10 s. Since the refocus process relies on image sharpness, an evaluation of the jitter influence is compulsory.

In our simulations, jitter is modelled as attitude misalignment for different captured frames: An optical beam is steered in a propagation simulation by applying a tilt to the wavefront [10]. As illustrated in Fig. 4, a tilt of angle α_x in the *x*-*z* plane and α_y in the *y*-*z* plane, where the *z*-axis is the Sun direction, will result in an off-pointing direction of the wavefront. The phase function for producing this tilt is

$$\phi = k\left[x\tan(\alpha_x) + y\tan(\alpha_y)\right], \tag{2}$$

where k is the wavenumber. Considering the formulation by Noll [12], this phase can be expressed as a linear combination of the two Zernike polynomials that account for a tilt aberration, Z_2 and Z_3, with coefficients $c_2 = ½ \tan(\alpha_x)$ and $c_3 = ½ \tan(\alpha_y)$.

Pointing errors in the spacecraft are simulated by displacements ρ (see left diagram of Fig. 4). They follow a circular normal distribution with given RMS(ρ) and equally probable arbitrary directions. If we consider $\rho = (x^2 + y^2)^{1/2}$, where x and y follow normal distributions with equal standard deviations σ, the standard deviation of a circular normal distribution is $\sigma_\rho = ½ \sigma (2 - \pi/2)$ [13].

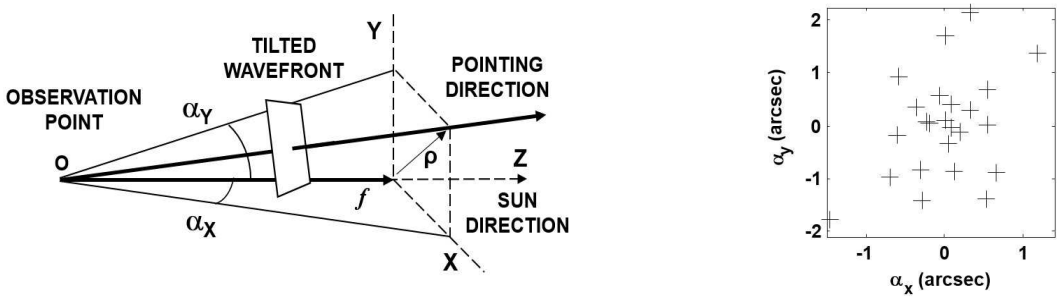

Fig. 4. Left: The pointing direction of the wavefront modelled is tilted with respect to Sun orientation. Right: Angular deviations of line of sight during an image accumulation of 24 frames following a circular normal distribution with σ_ρ=0.5 arcsec.

We will consider a RMS(ρ)=0.5 arcsec within 10 s for the jitter and an accumulation of 24 frames at 100 ms frame rate requirement for image acquisition. However we will assume this RMS during the 2.4 s image formation in our simulations for an oversize estimation of image degradation by jitter. The right plot of Fig. 4 shows the α_x and α_y angles calculated for producing F=24 tilted wavefronts following a circular normal distribution with σ_ρ=0.5 arcsec.

The aberration phase, given by each pair of angles, is used to build an OTF. The frame I_{jit} corresponding to this off-pointing direction is produced by multiplying the Fourier transform of the reference image by this OTF. Finally, an accumulated image I_{acc} of F frames, is formed by the average

$$I_{acc} = \frac{1}{F} \sum_{jit=1}^{F} I_{jit} \tag{3}$$

In our simulation we are thus assuming that the accumulation of F jittered frames eventually forms one image. The contrast of an image as a function of the RMS considered in its jitter is plotted in Fig. 5. As expected, the image contrast is reduced as the standard deviation of the circular normal distribution increases. In particular, for σ_ρ=0.5 the contrast of the accumulated image I_{acc} is 99.8% the one of the reference image. This reduction of contrast is considered negligible to complicate the FDT design with an image stabilization system (if jitter is kept within the RMS assumed). However, as seen in Fig. 5, the influence of jitter on image quality can be significant if RMS is further increased.

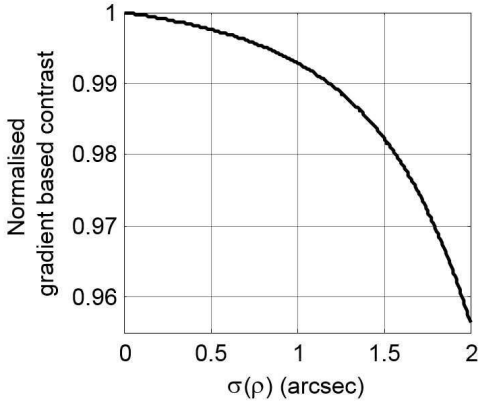

Fig. 5. Image contrast versus jitter as a function of the circular normal standard deviation.

VI. REFOCUS PROCESS SIMULATION

In this section a complete refocus process is simulated. As explained in Section IV, the figure of merit evaluates the image contrast, and this information will be used by the system to locate the best focus position. To evaluate the robustness of this method a relation between L2 displacements and pure defocusing was derived. Then a sequence of defocused images as a function of this excursion were generated.
The number of waves of defocus (δ) at the edge of the pupil is related to the defocus distance as $\Delta z=8\lambda\,\delta\,(F\#)^2$, where *F#* is the *f*-number of the optical system and λ the wavelength [14]. This relation can be compared to the expression of the fourth Zernike polynomial, the one that accounts for defocus, and the following expression can be derived

$$\Delta z = -\frac{8\sqrt{3}}{\pi}\lambda\left(F\#\right)^2 c_4 \tag{4}$$

where c_4 is the fourth Zernike coefficient. Thus, pure defocus by a lens displacement Δz can be modelled as a wavefront error proportional to the Zernike polynomial Z_4. This polynomial is included in the aberration phase.

Thus, the OTF computed includes the defocus aberration, via the Z_4 polynomial, and the jitter contribution, as described in Section V. Moreover, the accuracy of the L2 position set by the mechanism is ±10μm and, consequently, this position uncertainty may affect the performance of the refocusing process. This is also provided in the OTF by adding an uncertainty to the lens displacement of Δz±10μm, at any position of L2, with a square probability density function.

Following this procedure, a sequence of 37 OTFs were generated. They correspond to defocus distances in the range of ±2 mm in 110 μm steps. They also included jitter and position uncertainty in the computation as explained. When these transfer functions are multiplied by the Fourier transform of the reference image, a set of images result. They correspond to a simulation of the image degradation, as a function of the lens displacement, i.e. during the refocusing process. Fig. 3a) and c) are a close up of the images generated for Δz=0, and Δz=1.76 mm (plus uncertainties), respectively.

Finally, the masked-gradient based algorithm was applied to this set of images and its normalized values are shown in Fig. 6 as a function of the lens position. The curve, plotted as a solid line, covers the dynamic range in a smooth way, even in the presence of 'noise' given by the mechanical uncertainties. Within the focal depth range the contrast variation is quite significant and thus easy to detect. This implies a wide margin of error against mechanical instabilities in L2 or lack of precision in the position of the maximum contrast. Nevertheless, in practice, it is expected that the excursion of the lens will induced more aberrations than pure defocus and indeed the presence of other aberrations can destroy the symmetry of this curve. However their contribution is small against the induced defocus and we have neglected them in our study. Thus, the refocusing system looks for the image plane with the sharpest image (i.e. highest contrast or best focus) rather than for the position with the minimum defocus aberration.

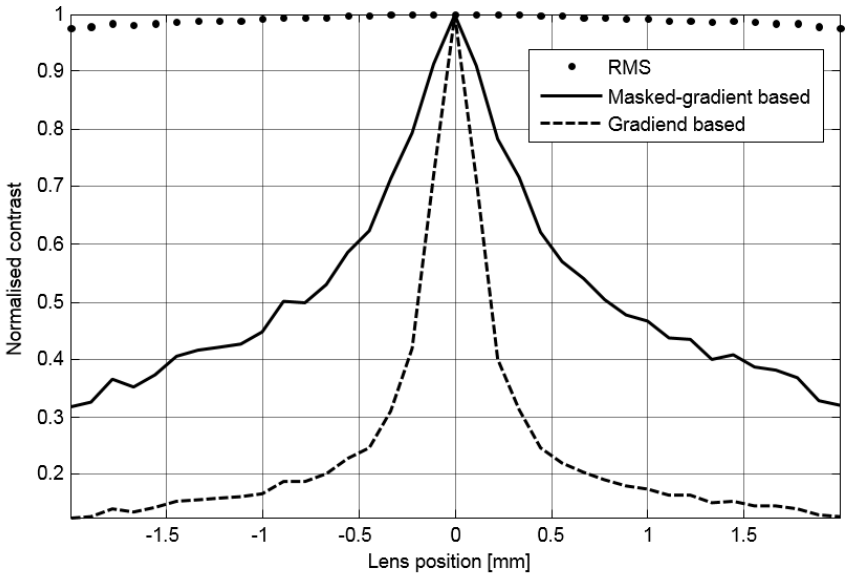

Fig. 6. Contrast computed from a sequence of images using different figures of merit. The images are obtained numerically and correspond to the L2 excursion along the scanning range of the FRM, where defocus, jitter and mechanical instabilities are simulated. The image RMS is plotted as a dotted curve, the gradient based contrast as a dash line and the masked-gradient based contrast as a solid line.

For comparison purposes, other figures of merit are illustrated in Fig. 6. The image RMS is plotted as a dotted line. It is also a common figure of merit used to measure image contrast but, as it is illustrated, it provides very low sensitivity to contrast variation in our system. Alternatively, the gradient-based contrast without the cancelling mask, and plotted as a dashed line, provides good sensitivity for small defocused states. However, the curve has long flat wings within the scanning range, which can compromise the refocusing process. Moreover, since the mask is not applied, the contrast can be more sensitive to solar features such as prominences or filaments.

VII. CONCLUSION

The proposed autofocus system is sufficiently robust against mechanical uncertainties and expected lateral image shifts. The masked gradient-based contrast algorithm, which performs a contrast evaluation restricted to the solar limb, has proved to be the most convenient criteria for the autofocus system of the FDT.

ACKNOWLEDGEMENTS

The authors would like to thank the Spanish government for the support of this research via the grants AYA2012-39636-C06-01, “Diseño detallado, fabricación e integración de SO/PHI” and ESP2013-47349-C6-2R, “Fabricación e integración de SO/PHI”.

REFERENCES

[1] A. Gandorfer, S.K. Solanki, J. Woch, V. Martínez Pillet, A. Álvarez Herrero and T. Appourchaux, “The Solar Orbiter Mission and its Polarimetric and Helioseismic Imager (SO/PHI),” Journal of Physics: Conference Series 271 (2011), 012086.
[2] Y. Michel, E. Conde, D. Kouach, M. Simpfendoerfer, Y. Parot, G.R. Orttner, M. Saccoccvio and S. Maurice, “Chemcam screwnut autofocus mechanism: qualification data and guidelines for space-use of ground equipments,” Proc. 13th European Space Mechanisms and Tribology Symposium- (ESMATS 2009).
[3] A. Álvarez-Herrero, “The polarization modulators based on liquid crystal variable retarders for the PHI and METIS instruments for the Solar Orbiter mission”, proceeding 66598 at International Conference on Space Optics (ICSO 2014).
[4] V. Martínez-Pillet, J.C. del Toro-Iniesta, A. Alvarez-Herrero, et al., “The Imaging Magnetograph eXperiment (IMAX) for the Sunrise Balloon-Borne Solar Observatory,” Solar Phys, 2011, 268, pp. 57-102.
[5] D. Garranzo, “Optical performance of the SO/PHI Full Disk Telescope due to temperature gradient effects on the Heat Rejection Entrance Windows”, proceeding 66269 at International Conference on Space Optics (ICSO 2014).
[6] J. Barandiarán, “Solar Orbiter/ PHI Full Disk Telescope Entrance Window mechanical mount”, proceeding 66273 at International Conference on Space Optics (ICSO 2014).
[7] R.C. Gonzalez, R.E. Woods, S.L. Eddins, *Digital image processing using Matlab*. Tata McGraw Hill, 2010.
[8] P.H. Scherrer, J. Schou, R.I. Bush, A.G. Kosovichev, R. S. Bogart, J. T. Hoeksema, Y. Liu, T. L. Duvall Jr., J. Zhao, A. M. Title, C. J. Schrijver, T. D. Tarbell and S. Tomczyk, “The Helioseismic and Magnetic Imager (HMI) investigation for the Solar Dynamics Observatory (SDO),” Solar Phys, 2012, pp. 207-227.
[9] J.W. Goodman, *Introduction to Fourier optics*, McGraw-Hill International Editions, 1996.
[10] D. Voelz, *Computational Fourier optics: a Matlab tutorial*, SPIE Press 2011.
[11] Y. Katsukawa, Y. Masada, T. Shimizu, S. Sakai and K. Ichimoto, “Pointing stability of Hinode and requirements for the next solar mission Solar-C,” proceeding at International Conference on Space Optics (ICSO 2010).
[12] R.J. Noll, “Zernike polynomials and atmospheric turbulence,” J. Opt. Soc. vol. 66, 1976, pp. 207-211.
[13] P. Mathews and M. Malnar and Bailey, Inc. “The circular normal distribution,” unpublished.
[14] R.G. Paxman and J. R. Fienup, “Optical misalignment and image reconstruction using phase diversity,” J. Opt. Soc. Am. A, vol. 5, pp. 914-923.